ADVANCING EARTH AND SPACE SCIENCES

JGR Space Physics

RESEARCH ARTICLE

10.1029/2022JA031209

Key Points:

- Three-dimensional kinetic simulations are used to study reconnection with a finite x-line length
- Electron inertia term plays a crucial role at the two edges of x-line in the current direction
- The features of Hall effect, plasma flow, and plasma heating are different between the dawn and dusk side of the x-line

Correspondence to:

Q. Lu,
qmlu@ustc.edu.cn

Citation:

Huang, K., Lu, Q., Liu, Y.-H., Lu, S., & Wang, R. (2023). Characteristics of magnetic reconnection with a finite x-line length. *Journal of Geophysical Research: Space Physics*, *128*, e2022JA031209. https://doi.org/10.1029/2022JA031209

Received 6 DEC 2022
Accepted 14 JUL 2023

Characteristics of Magnetic Reconnection With a Finite X-Line Length

Kai Huang[1,2,3], Quanming Lu[1,2,3], Yi-Hsin Liu[4], San Lu[1,2,3], and Rongsheng Wang[1,2,3]

[1]Deep Space Exploration Laboratory/School of Earth and Space Sciences, University of Science and Technology of China, Hefei, China, [2]CAS Center for Excellence in Comparative Planetology/CAS Key Lab of Geospace Environment, University of Science and Technology of China, Hefei, China, [3]Collaborative Innovation Center of Astronautical Science and Technology, Harbin, China, [4]Department of Physics and Astronomy, Dartmouth College, Hanover, NH, USA

Abstract The characteristics of magnetic reconnection with a finite x-line length are studied using three-dimensional (3D) particle-in-cell (PIC) simulations. We simulate two cases: anti-parallel reconnection and guide field reconnection. In both cases, reconnection is triggered by an initial perturbation that is localized in the current direction, and then, an active reconnection region extending around 20 ion inertia length along the current direction is developed. In both cases, the electron inertia term plays an important role in balancing the reconnection electric field near the two edges of the x-line along the current direction. On the ion drifting side, ions are heated while electron heating is not significant; while on the electron drifting side, electrons are heated while ion heating is weak. In the anti-parallel case, the out-of-plane Hall magnetic field on the ion and electron drifting side of the reconnection region shows reversed polarization, while in the guide field case, the in-plane Hall electric field shows reversed polarization. These features can be used as identifications for reconnection with a finite x-line length during observations in the magnetotail, they also provide an estimation of the satellite location in the dawn-dusk direction of the reconnection region.

1. Introduction

Magnetic reconnection in space plasma is believed to be responsible for various explosive phenomena, such as solar flares (Giovanelli, 1946; Masuda et al., 1994), coronal mass ejections (Chen, 2011; Shibata et al., 1995), and magnetospheric substorms (Angelopoulos et al., 2008; Birn et al., 2011). During reconnection, the magnetic field lines on the two sides of the current sheet can "break" and "reconnect" at the x-line, where the magnetic connectivity is changed (Hesse & Schindler, 1988; Vasyliunas, 1975). Meanwhile, magnetic energy is rapidly converted to plasma kinetic and thermal energy. Most of our understanding of magnetic reconnection are learned from two-dimensional (2D) models, where all quantities are translational invariant along the out-of-plane direction (i.e., the x-line direction or the current direction), and therefore the reconnection x-line is infinitely long. However, in many space environments, the reconnection region is localized in the current direction, and the length of the reconnection x-line is finite and comparable to the plasma kinetic scale (tens of ion inertia length).

The planetary magnetosphere provides a natural environment for the development of magnetic reconnection with a finite x-line length. In some small planets, the reconnection x-line length is limited by the spatial scale of the magnetosphere. For example, the dawn-dusk scale of the thin current sheet and reconnection site at Mercury's magnetotail is around 40 ~ $60d_i$ (d_i is the ion inertia length) (Rong et al., 2018; Sun et al., 2016, 2021). For planets with large magnetosphere, like Earth, reconnection with a finite x-line length is also expected to occur under localized drivers. Observations have indicated that bursty bulk flows (BBFs) and dipolarization fronts (DFs) in the magnetotail are localized in the dawn-dusk direction with a typical length of several R_E (Huang et al., 2015; Liu et al., 2013, 2015; Nakamura et al., 2004, 2005). These structures are believed to be generated by magnetic reconnection that has a finite x-line length (Shay et al., 2003) or the break of a large-scale reconnection outflow through electron flow shear instability (Fujimoto, 2016) or kinetic ballooning/interchange instability (Pritchett et al., 2014). Reconnection with a finite x-line length can also develop in numerical simulations. Through three-dimensional (3D) two-fluid simulations including the Hall term and electron inertia, Shay et al. (2003) studied the onset and evolution of magnetic reconnection from random perturbations. They found that initially the reconnection x-lines have finite lengths, and these localized reconnection x-lines are kept to be isolated for a long time when the initial current sheet is thick (~$2d_i$). Pritchett and Lu (2018) studied magnetic reconnection in a magnetotail equilibrium using 3D particle-in-cell (PIC) simulations. They find that a high-latitude, localized driving E_y field can trigger localized magnetotail reconnection with a finite x-line length. Therefore, while magnetic reconnection with a finite x-line length is ubiquitous, its characteristics are rarely studied.

Previous simulations also showed that reconnection with a finite x-line length behaves greatly different from that in 2D conditions. Nakamura et al. (2012) performed 3D Hall magnetohydrodynamic (MHD) simulations to study magnetic reconnection with a finite width along the current direction. They found that the reconnection region can spread in the current direction, and the spreading speed at the ion/electron drifting side is almost equal to the ion/electron flow velocity that carries the current (Similar spreading persists during reconnection with a guide field [Shepherd & Cassak, 2012]). They also found that the reconnection jets and Hall magnetic field structures show asymmetric distribution along the x-line direction. Huang et al. (2020) and Liu et al. (2019) studied magnetic reconnection with a finite x-line extent using 3D PIC simulations. The initial condition is a modified Harris current sheet that is thin in the center and thick on the two sides along the current direction, and therefore the reconnection region can be spatially confined in the thin current sheet without shifting and spreading. They found that an internal x-line asymmetry develops where reconnection is active on the electron drifting side while it is suppressed in a region around $10d_i$ along the x-line direction on the ion drifting side. Both the average reconnection rate and outflow speed are found to be decreased when the length of the x-line becomes shorter, and reconnection is completely suppressed when the x-line is shorter than around $10d_i$.

In this paper, using 3D PIC simulations, we study the characteristics of magnetic reconnection with a finite x-line length. The initial setup in Huang et al. (2020) and Liu et al. (2019) is limited to the anti-parallel reconnection condition. Here, the localized reconnection x-line is obtained by introducing a localized initial perturbation along the current direction, this setup enables us to consider both the anti-parallel reconnection and reconnection with a guide field. Compared with previous studies, we will further focus on electron kinetic signatures of reconnection. The results may have potential applications on localized reconnection in a large current sheet such as Earth's magnetotail reconnection, and serve as identifications for reconnection with a finite x-line length during observations.

2. Simulation Setup

The simulations in this work are performed using the 3D PIC code VPIC, an open-source project which has been successfully used to numerically study plasma physics (Bowers, Albright, Bergen, et al., 2008; Bowers, Albright, Yin, et al., 2008; Bowers et al., 2009). The initial configuration is a Harris sheet with magnetic field $\mathbf{B}(z) = B_0 \tanh(z/\delta_0)\mathbf{e}_x + B_g\mathbf{e}_y$ and plasma density $n(z) = n_0\mathrm{sech}^2(z/\delta_0) + n_b$. Here, B_0 is the asymptotic magnetic field, δ_0 is the half-thickness of the current sheet, n_0 is the peak density of the current sheet, $n_b = 0.05n_0$ is the background density. The initial distributions of ions and electrons are Maxwellian while the current sheet populations have drift velocities along the y direction $-V_{i0}/V_{e0} = T_{i0}/T_{e0} = 5$ to satisfy the Ampere's law $\nabla \times \mathbf{B} = \mu_0\mathbf{J}$. Ions drift to the $+y$ direction, while electrons drift to the $-y$ direction. Ion to electron mass ratio is set to be $m_i/m_e = 100$. The light speed is $c = 20V_A$, where V_A is the Alfvén speed defined by $V_A = B_0/\sqrt{\mu_0 m_i n_0}$. The upstream Alfvén speed defined by $V_{Ab} = B_0/\sqrt{\mu_0 m_i n_b} \approx 4.5V_A$ is used for the normalization of the electric field. The simulation domain is centered at $x = y = z = 0$ and the size is $L_x \times L_y \times L_z = 32d_i \times 64d_i \times 16d_i$ with a spatial resolution $\Delta x = \Delta y = \Delta z = 0.05d_i \approx 3.5\lambda_{De}$, here, d_i is the ion inertia length based on n_0, λ_{De} is the electron Debye length in the current sheet. We use the ion gyro-frequency $\Omega_i \equiv eB_0/m_i$ for the normalization of time. Over 2.6×10^{10} particles for each species are used in our simulations. An initial perturbation on the magnetic field is introduced to trigger the reconnection. The perturbation is centered at $(x, y, z) = (0, 0, 0)$ and spatially localized in the y direction with a length L_{pert}. The detailed form is $\delta B_x = \partial\Psi/\partial z$, $\delta B_z = -\partial\Psi/\partial x$, where

$$\Psi = -\Psi_0 \frac{\left(L_{cx}^{-1}\sin\left(2\pi|x|/L_x\right) + 2\pi L_x^{-1}\cos\left(2\pi x/L_x\right)\right)\cos\left(\pi z/L_z\right)\exp\left(-|x|/L_{cx} - z^2/L_{cx}^2\right)}{L_{cx}^{-2} + 4\pi^2 L_x^{-2}} f(y), \quad \text{and} \quad f(y) = \frac{\tanh\left(y + 0.5L_{pert}\right) - \tanh\left(y - 0.5L_{pert}\right)}{2tanh\left(L_{pert}/2L_{trans}\right)},$$

here, $L_{cx} = 0.1L_x$, $L_{cz} = 0.5L_z$, and $L_{\mathrm{trans}} = 2d_i$. We set Ψ_0 to ensure the peak of δB_z is $0.05B_0$. In the x and y direction, we use periodic boundary conditions, while in the z direction, conducting boundary conditions are used for electromagnetic field, reflecting boundary conditions are used for particles.

We run two cases in this paper, Case 1 is anti-parallel reconnection, while Case 2 is reconnection with a guide field. Detailed differences on the parameters between these two cases are summarized in Table 1. Although L_{pert} is different in the two cases, the active reconnection region has a similar length in the two cases when reconnection is well developed. We focus on the characteristics of the reconnection region, not the evolution of the length of

Table 1
Some Simulation Parameters for Case 1 and Case 2

Parameter name	Case 1	Case 2
Guide field B_g	0	B_0
Half-thickness of the current sheet δ_0	$1.0d_i$	$0.75d_i$
Length of the initial perturbation L_{pert}	$30d_i$	$20d_i$

the reconnection x-line, this is the reason for the different parameters in the two cases.

3. Simulation Results

3.1. Anti-Parallel Reconnection

First, we analyze the results from the anti-parallel case. Figure 1 shows the reconnected magnetic field B_z on the $z = 0$ plane at $\Omega_i t = 0$, 20, 30, 35, and 40 respectively. The initial B_z perturbation is introduced between $y = \pm 15d_i$ as labeled by the horizontal dashed lines. In our simulations, a B_z reversal from negative to positive along the $+x$ direction implies a reconnection x-line. Therefore, we use the B_z patterns on the $x - y$ plane to identify the time evolution of the reconnection region. As the evolution of reconnection, the reconnection region with B_z reversal gradually shifts to the ion drifting ($+y$) direction. The region with the initial B_z perturbation extends $30d_i$ along the y direction, while the reconnection region extends only around $20d_i$ in the later stage. The shorten of the reconnection region is similar to the internal x-line asymmetry developed in a localized thin current sheet (Huang et al., 2020; Liu et al., 2019), where a suppression region around $10d_i$ is formed on the ion drifting side, and therefore the active reconnection region becomes shorter compared with the initial perturbation. At $\Omega_i t = 35$, some small-scale finger structures with a wave length around $1 \sim 2d_i$ develop along the outer boundaries of the reconnection fronts. These structures are generated by ballooning/interchange instability (BICI), and have been discussed in Pritchett and Coroniti (2010) and Pritchett (2016). Hereafter, we will focus on the time slice $\Omega_i t = 32$, when the reconnection rate reaches the maximum.

Figure 2 shows some typical quantities in the reconnection region. Panels (a-d) plot the reconnected magnetic field B_z, reconnection electric field E_y, electron outflow velocity V_{ex}, and ion outflow velocity V_{ix} on the $z = 0$ plane. Here the active reconnection region is identified by the region where the half-thickness of the current sheet δ (half of the full width at half maxima of the profile of J_y) is less than the local electron inertia length $d_{e,l}$ along $x = 0$, as bounded by the two horizontal dashed lines (Huang et al., 2020). In this region, the reconnection electric field has large amplitudes, and there is a reversal in the reconnected magnetic field, the electron and ion outflows, consistent with the typical signatures of reconnection.

In Figure 3, we analyze the generalized Ohm's law along the reconnection x-line. To reduce the numerical noises, the terms in the generalized Ohm's law are time averaged during a period of $1\Omega_i^{-1}$. Along the x-line in anti-parallel reconnection, the magnetic field is around zero, and the reconnection electric field is mainly balanced by the electron pressure tensor and inertia terms, $\mathbf{E} = -\nabla \cdot \mathbf{P}_e/en - (m_e/e)\mathrm{d}\mathbf{V}_e/\mathrm{d}t$. Panel (a) shows the reconnection electric field E_y on the $x = 0$ plane, while panel (b) plots the line profile of E_y, the y component of $\nabla \cdot \mathbf{P}_e/en$ and $(m_e/e)\mathrm{d}\mathbf{V}_e/\mathrm{d}t$

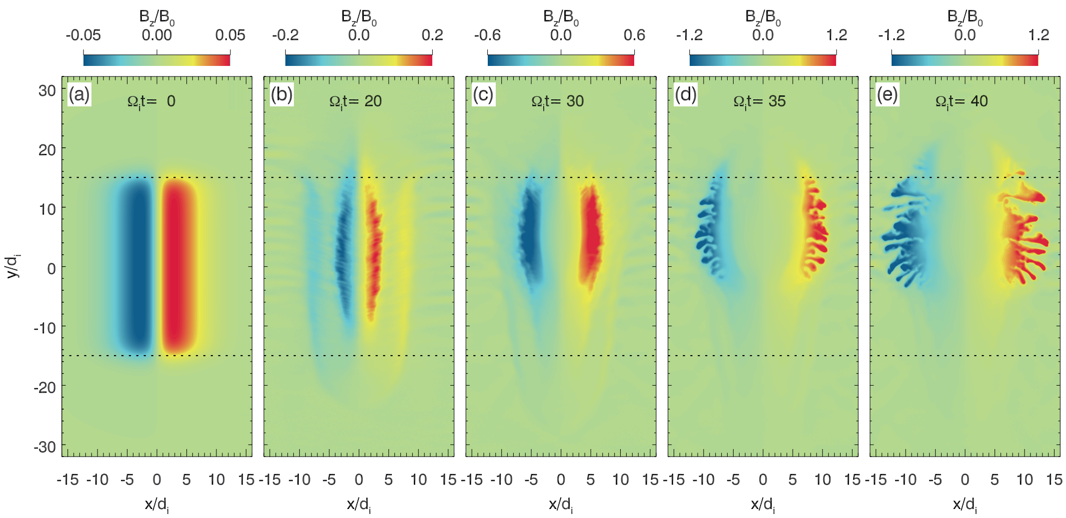

Figure 1. The reconnected magnetic field B_z/B_0 on the $z = 0$ plane at $\Omega_i t = 0$, 20, 30, 35, and 40, respectively. The two horizontal dashed lines label the region with the initial perturbation.

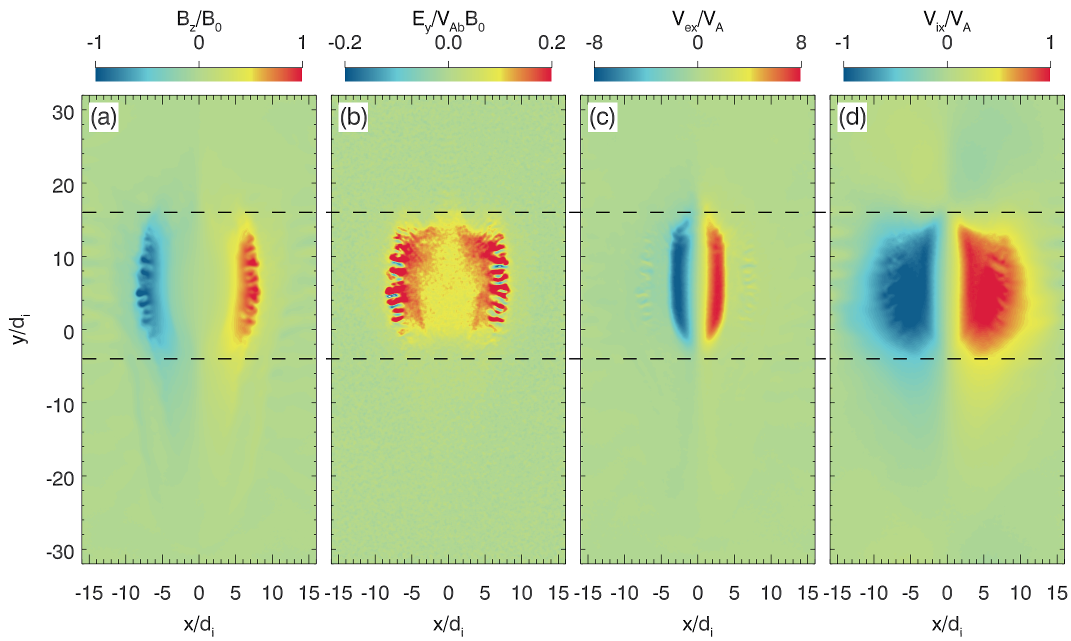

Figure 2. Some typical quantities at $\Omega_i t = 32$. Panels (a–d) show the reconnected magnetic field B_z/B_0, the reconnection electric field $E_y/V_{Ab}B_0$, the electron outflow velocity V_{ex}/V_A, and the ion outflow velocity V_{ix}/V_A on the $z = 0$ plane. The two horizontal dashed lines label the active reconnection region.

along the x-line. Panel (c) plots the half-thickness of the current sheet $\delta/d_{e,l}$ and the electron velocity V_{ey} as a reference of the active reconnection region, which is bounded by the two vertical dashed lines. We find that the in the central reconnection region, E_y is nearly uniform and is mainly balanced by the electron pressure tensor term, while the electron inertia term is negligibly small. The amplitude of E_y normalized by the upstream magnetic field and Alfvén speed is around 0.1. These results are consistent with previous 2D simulations (Cassak et al., 2017; Hesse et al., 2011; Pritchett, 2001; Zenitani et al., 2011). However, at the two edges of the x-line (around $y \approx -2d_i$ and $16d_i$), the amplitude of the electron inertia term is large and comparable to that of the electron pressure tensor term. At the edge on the $+y$ side, the electron inertia term has the same sign with the electron pressure tensor term, the reconnection electric field is balanced by the combination of the two terms. At the edge on the $-y$ side, the electron inertia term has the different sign with the electron pressure tensor term, and cancels some of the contribution of the electron pressure tensor term to the reconnection electric field. We argue that this signature that is greatly different from 2D reconnection persists even in the condition with a realistic mass ratio. The y component of the electron inertia term can be expressed as $(m_e/e)(\mathrm{d}\mathbf{V}_e/\mathrm{d}t)_y = (m_e/e)(\partial_t V_{ey} + V_{ex}\partial_x V_{ey} + V_{ey}\partial_y V_{ey} + V_{ez}\partial_z V_{ey})$. In 2D conditions, the ∂_y term vanishes, V_{ex} and V_{ez} are close to zero at the x-line. Then, $(m_e/e)(\mathrm{d}\mathbf{V}_e/\mathrm{d}t)_y = (m_e/e)\partial_t V_{ey}$, this term is negligible in the condition of a realistic mass ratio when the time variation is not large. However, in 3D conditions, the ∂_y term becomes effective, especially when the reconnection x-line has a finite length. In Figure 3c, we note that in the active reconnection region, the electron velocity V_{ey} reaches up to the electron Alfvén speed $V_{Ae} = 10V_A$, while in the current sheet outside the active reconnection region, V_{ey} is less than V_A. Therefore, the electron flow velocity has a great change near the two edges of the x-line along the y direction. From Figure 3c, we estimate that the amplitude of V_{ey} increases from 0 to V_{Ae} in a distance around $L = 5d_i$. Then, the ∂_y term can be scaled as $(m_e/e)V_{ey}^2/2L = 0.1(m_e/e)V_{Ae}^2/d_i = 0.1V_A B_0 \approx 0.022V_{Ab}B_0$. Obviously, the inertia term arising from the change of V_{ey} along the x-line also plays an important role in breaking the frozen-in condition at the edges. This conclusion is also insensitive to the current carrier, if the current is mainly carried

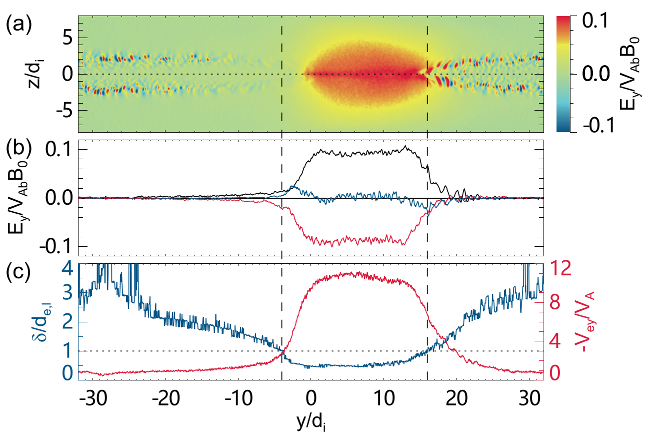

Figure 3. Panel (a) shows the reconnection electric field $E_y/V_{Ab}B_0$ on the $x = 0$ plane. Panel (b) plots the line profiles of E_y (black line), the y component of $\nabla \cdot \mathbf{P}_e/en$ (red line) and $(m_e/e)\mathrm{d}\mathbf{V}_e/\mathrm{d}t$ (blue line) along the x-line. Panel (c) plots the half thickness of the current sheet $\delta/d_{e,l}$ (blue line) and the amplitude of V_{ey} (red line) along the x-line. The two vertical dashed lines show the active reconnection region.

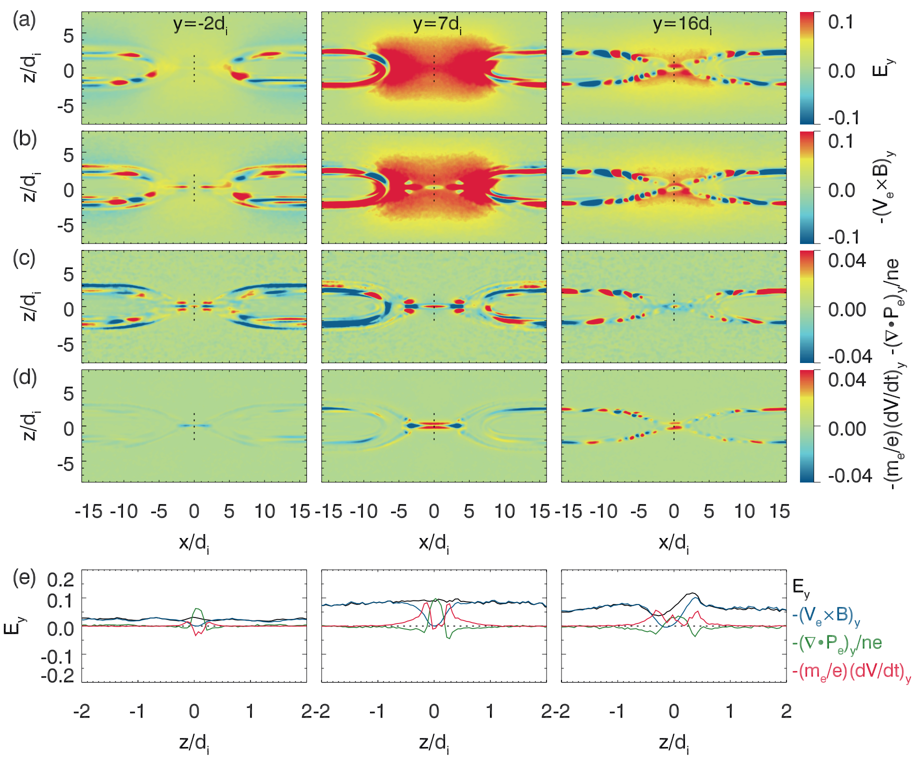

Figure 4. Panels (a–d) show the distribution of the reconnection electric field E_y, the y component of $-\mathbf{V}_e \times \mathbf{B}$, $-\nabla \cdot \mathbf{P}_e/en$ and $-(m_e/e)\mathrm{d}\mathbf{V}_e/\mathrm{d}t$ on the $y/d_i = -2$, 7, and 16 planes. Quantities are normalized by $V_{Ab}B_0$. Panel (e) plots the line profiles of these quantities along the vertical dashed lines in panels (a–d).

by electrons, the initial electron drift velocity is around V_A, still much smaller than the typical electron velocity V_{Ae} at the active x-line. Note the E_y fluctuations at around $z = \pm 2d_i$ in panel (a) are generated through lower hybrid drift instability due to the density gradient at the flanks of the current sheet (Daughton, 2003; Huba et al., 1977; Krall & Liewer, 1971), and is not the focus in this work.

Figure 4 presents the detailed distribution of the terms in the generalized Ohm's law on three planes $y/d_i = -2$, 7, and 16 respectively. The three columns correspond to the electron drifting side edge, center, and ion drifting side edge of the reconnection region. We find that the electron frozen-in condition is violated around the electron diffusion region (EDR) and the separatrix region, where the electron pressure tensor term and electron inertia term have significant amplitudes. Panel (*e*) plots the line profiles of the terms in the generalized Ohm's law cross the x-line along $x = 0$ in the three planes $y/d_i = -2$, 7, and 16 respectively. The balance of the generalized Ohm's law in the second column is similar to that in 2D simulations (Hesse et al., 2011; Pritchett, 2001; Zenitani et al., 2011): In the central EDR, reconnection electric field is balanced by the pressure tensor term, while at the boundary of EDR, electron inertia term dominates. However, at the two edges of the x-line along y direction, the electron inertia term in the central EDR cannot be ignored, as described in Figure 3.

The quadrupolar Hall magnetic field is an important signature in the ion diffusion region of collisionless magnetic reconnection (Eastwood et al., 2010; Øieroset et al., 2001). Figure 5 shows the out-of-plane magnetic field and in-plane current density on three planes $y/d_i = -2$, 7, and 16, respectively, corresponding to the electron drifting side edge, center, and ion drifting side edge of the reconnection region. Here, the in-plane current density is defined as $J_{in} = \mathrm{sgn}(J_x)\sqrt{J_x^2 + J_z^2}$, where sgn $(J_x) = 1$ when $J_x > 0$ and sgn $(J_x) = -1$ when $J_x < 0$. On the $y = 7d_i$ plane, except the separatrix region, quadrupolar out-of-plane magnetic field also displays around the reconnection fronts, while the polarity is opposite to that in the separatrix region, as shown in panel (a), this feature is similar to that in 2D conditions. The Hall magnetic field in the separatrix region is associated with the Hall current system carried by electrons, where electrons flow toward the x-line along the separatrices and flow away from the x-line along the magnetic field in the outflow region (Lu et al., 2010; Nagai et al., 2001; Pritchett, 2001). The out-of-plane magnetic field around the reconnection front is associated with the current

10.1029/2022JA031209

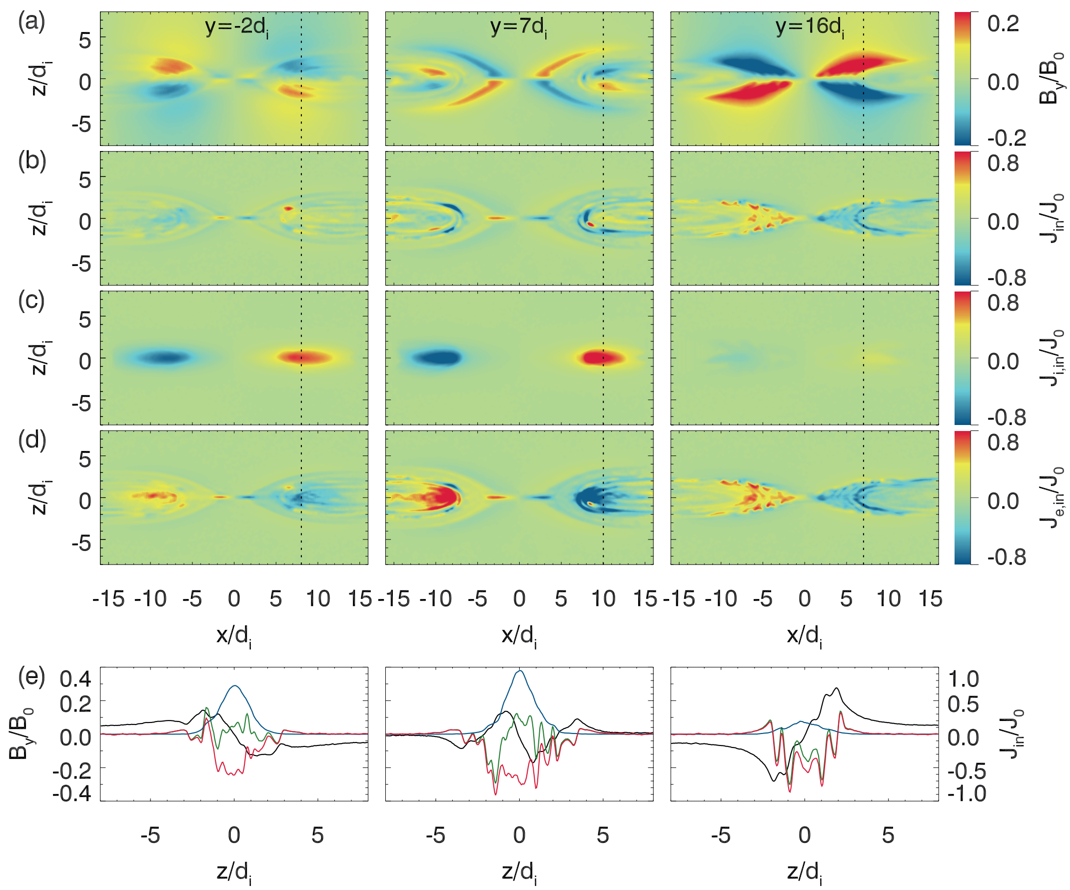

Figure 5. Panels (a–d) show the out-of-plane magnetic field B_y/B_0, in-plane current density J_{in}/J_0, in-plane ion current density $J_{i,in}/J_0$, and in-plane electron current density $J_{e,in}/J_0$ on the $y/d_i = -2$, 7, and 16 planes, where $J_0 = en_0V_A$. Panel (e) plots the line profiles of B_y/B_0 (black), J_{in}/J_0 (green), $J_{i,in}/J_0$ (blue), and $J_{e,in}/J_0$ (red) along the vertical dashed lines in panels (a–d).

carried by ions reflected at the front (Huang et al., 2014; Wang et al., 2022; Wu & Shay, 2012). However, on the ion drifting side of the reconnection region, the Hall magnetic field in the separatrix region become stronger, and the quadrupolar magnetic field around the reconnection fronts almost disappears; while on the electron drifting side, the quadrupolar magnetic field around the reconnection fronts dominates. This feature can be explained by different contribution between electrons and ions on the in-plane current at different locations in the reconnection region (see panels (b-e)). Panel (*e*) plots the line profiles of the out-of-plane magnetic field and in-plane current density along the vertical dashed lines in panels (a–d). At the central reconnection region ($y = 7d_i$ of panel (e)), the in-plane current density is dominated by electrons far from the current sheet ($|z| > 1d_i$), while it is dominated by ions in the central current sheet. Therefore, both the quadrupolar magnetic field around the separatrix and reconnection fronts can be formed. On the ion drifting side ($y = 16d_i$), the in-plane current density is dominated by electrons, forming the Hall magnetic field in the separatrix region. On the electron drifting side ($y = -2d_i$), the in-plane current density is dominated by ions, forming the out-of-plane magnetic field with polarity opposite to the Hall quadrupolar fields. The reason for this asymmetric distribution of the in-plane current along the y direction is that the reconnected magnetic field B_z is transported to the electron drifting side (Huang et al., 2020; Liu et al., 2019), and therefore, the reconnection fronts and ion jets associated with the reflected ions are stronger than those on the ion drifting side. Similar distribution of the out-of-plane magnetic field was also observed in Nakamura et al. (2012) with 3D Hall MHD simulations, and was explained by the opposite directions of the deflected ion outflow jets on the two sides the reconnection region in the y direction.

Panels (a) and (b) in Figure 6 show the electron and ion temperatures on the $z = 0$ plane, the temperature is defined by $T = \mathrm{tr}(\mathbf{T})/3$ and $T_{ij} = m_s\Sigma(v_i - V_i)\,(v_j - V_j)/N$, where s represents species (electron or ion), $i, j = x$, y, z, Σ represents the sum over all the particles in one cell, and N is the total number of particles in one cell,

10.1029/2022JA031209

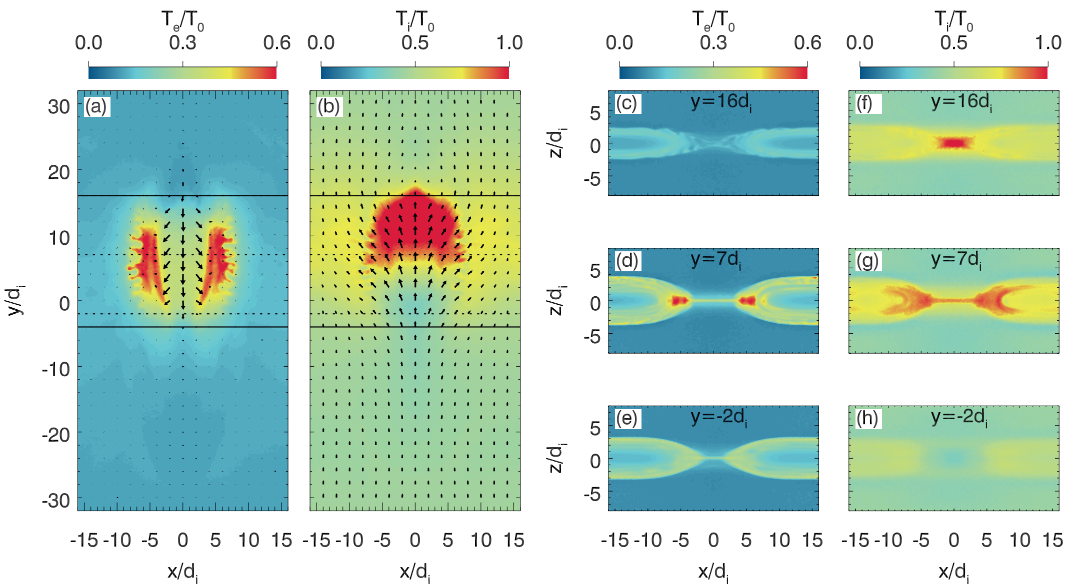

Figure 6. Panels (a) and (b) show the electron and ion temperatures on the $z = 0$ plane, the active reconnection region is bounded by the horizontal solid lines, and the arrows represent the in-plane flow vectors of the associated species. Panels (c)–(h) show the electron and ion temperatures on the $y/d_i = 16$, 7, and -2 planes, which are labeled by the horizontal dashed lines in panels (a) and (b).

$V_i = \Sigma v_i/N$ is the bulk velocity. Both electrons and ions are heated in the reconnection region, electron heating is predominated at the outflow region, while ion heating occurs in the entire reconnection layer. The temperature distribution of electron and ion along the y direction is also different, ions are more heated on the ion drifting side compared with electrons. Panels (c-h) show the electron and ion temperature on the $y/d_i = 16$, 7, and -2 planes, respectively, as denoted by the horizontal dashed lines in panels (a) and (b). On the $y = -2d_i$ plane, electrons are heated in the diffusion region, pile-up region and the outer edge of the magnetic island, while ions are only slightly heated in the magnetic island. On the $y = 7d_i$ plane, both electrons and ions are heated in the diffusion region. On the $y = 16d_i$ plane, ions are greatly heated while electron heating is negligible. Both electrons and ions can be heated by the electric field in the y direction during their drift motions. Electrons drift to the $-y$ direction while ions drift to the $+y$ direction, as shown by the flow vectors in panels (a) and (b), and therefore, electrons and ions are heated on the different side of the reconnection region along the y direction. We also note that there is region extending around $10d_i$ with low ion temperature in the diffusion region on the $-y$ direction, indicating that we may not observe ion heating in the diffusion region if the reconnection x-line is too short in the y direction.

3.2. Guide Field Reconnection

In this section, we present the results from reconnection with a guide field. Figure 7 shows the evolution of the reconnected magnetic field B_z on the $z = 0$ plane. In this case, the region with the initial perturbation extends $20d_i$ in the y direction. During reconnection, the reconnection region also shifts to the $+y$ direction, similar to that shown in Figure 1. However, the length of the reconnection region is almost unchanged. Therefore, although the length of the initial perturbation is different, the resulted reconnection regions extend around $20d_i$ in the y direction in both cases. We will focus on time slice $\Omega_i t = 28$, when the reconnection rate reaches the maximum.

In Figure 8, we analyze the generalized Ohm's law along the x-line, and the layout of this figure is similar to that in Figure 3 in the anti-parallel case. In the case with a guide field, we find that the electron inertia term associated with the increase and decrease of the electron drifting velocity V_{ey} also has significant amplitudes; it has the same sign with the electron pressure tensor term on the ion drifting side, and has the different sign on the electron drifting side. The difference compared with the anti-parallel case is that the electron inertia term is distributed not only at the two edges of the x-line, but also in a larger region. Even at the location where the reconnection electric field E_y reaches the peak value (at around $y = 15d_i$), the amplitude of the electron inertia term is also large. The wide distribution of the electron inertia term may be related to different electron dynamics in the guide

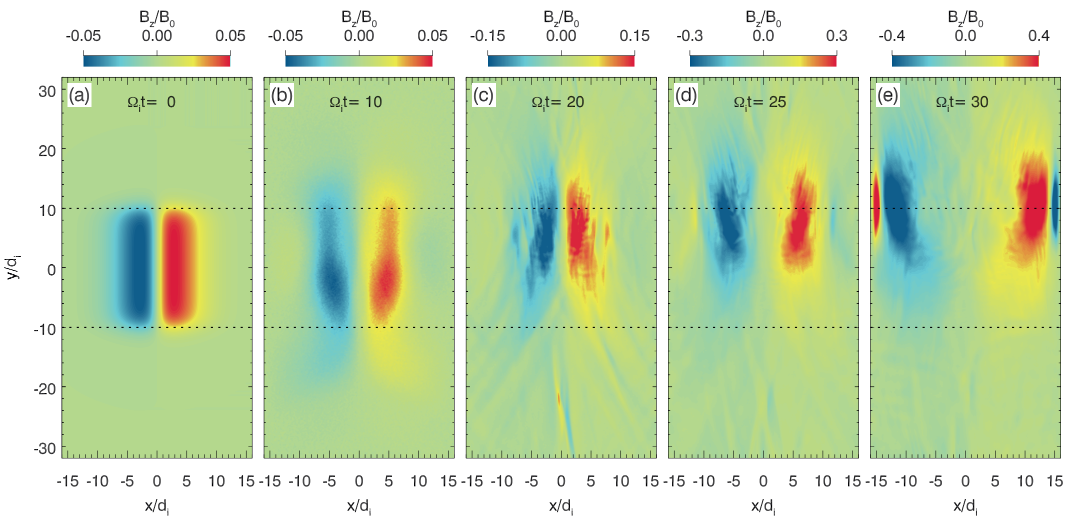

Figure 7. The reconnected magnetic field B_z/B_0 on the $z = 0$ plane at $\Omega_i t = 0$, 10, 20, 25, and 30, respectively. The two horizontal dashed lines label the region with the initial perturbation.

field case compared with that in the anti-parallel case. In the guide field case, electrons can be trapped within the EDR by the guide field, and obtain more acceleration by the parallel electric field, therefore, the spatial variation of V_{ey} distributes over a larger region. Previous 2D simulations found that the reconnection rate is reduced in the presence of a guide field (Huba, 2005; Ricci et al., 2004), however, the peak amplitude of E_y here is around 1.5 times of that in the anti-parallel case, while the average reconnection rates are comparable in the two cases. The reason is that the spatial variation of the amplitude of E_y along the x-line is much larger in the guide field case. This result suggests that when there is a guide field, quasi-2D assumptions could be invalid for the whole reconnection region in the case of a finite x-line length.

Figure 9 shows the electron current density J_{ey}, electron velocity V_{ex}, V_{ey}, and electric field E_z on the $y/d_i = 18$, 12, and 4 planes, respectively. The distributions of these quantities are greatly different along the y direction. On the ion drifting side, the electron current sheet is short and thick (panel (a)), while a long and thin electron current sheet is formed along the upper-left and lower-right separatrices toward the electron drifting side (panel (c)). Note that the reversal of the guide field direction will lead to the formation of a thin current sheet along the upper-right and lower-left separatrices. Similar result is also obtained during reconnection with a finite x-line length in a force-free current sheet with a guide field, and the elongated current sheet on the electron drifting side is unstable to the oblique tearing instabilities, forming secondary flux ropes (Daughton et al., 2011; Huang et al., 2022). Electron outflows away from the x-line are also distributed along these two branches of separatrices, as shown in panel (f), while on the ion drifting side, electron outflows are weak, the electron flows are dominated by electron inflows distributed along the upper-right and lower-left separatrices (panel (d)). Such kind of flow pattern is also accompanied by V_{ey} as shown in panels (g–i), on the ion drifting side, large V_{ey} appears along the upper-right and lower-left separatrices with electron inflows, while on the electron drifting side, large V_{ey} appears along the upper-left and lower-right separatrices with electron outflows. This asymmetric flow distribution results in the different Hall electric field E_z patterns on the ion and electron drifting side (panels (j–l)). Around the x-line, the bipolar E_z, which is mainly balanced by $-(\mathbf{V}_e \times \mathbf{B})_z$, points to the current sheet on the ion drifting side, while it points away from the current sheet toward the electron drifting direction. Previous 3D simulation with periodic boundary condition in the current direction (the x-line is infinitely long)

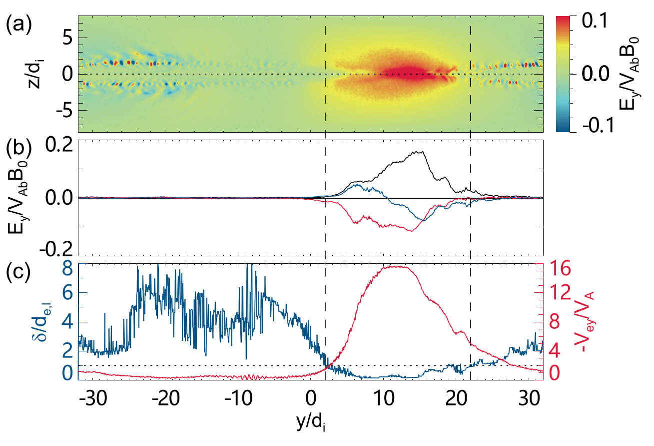

Figure 8. Panel (a) shows the reconnection electric field $E_y/V_{Ab}B_0$ on the $x = 0$ plane. Panel (b) plots the line profiles of E_y (black line), the y component of $\nabla \cdot \mathbf{P}_e/en$ (red line) and $(m_e/e)\mathrm{d}\mathbf{V}_e/\mathrm{d}t$ (blue line) along the x-line. Panel (c) plots the half thickness of the current sheet $\delta/d_{e,l}$ (blue line) and the amplitude of V_{ey} (red line) along the x-line. The two vertical dashed lines show the active reconnection region.

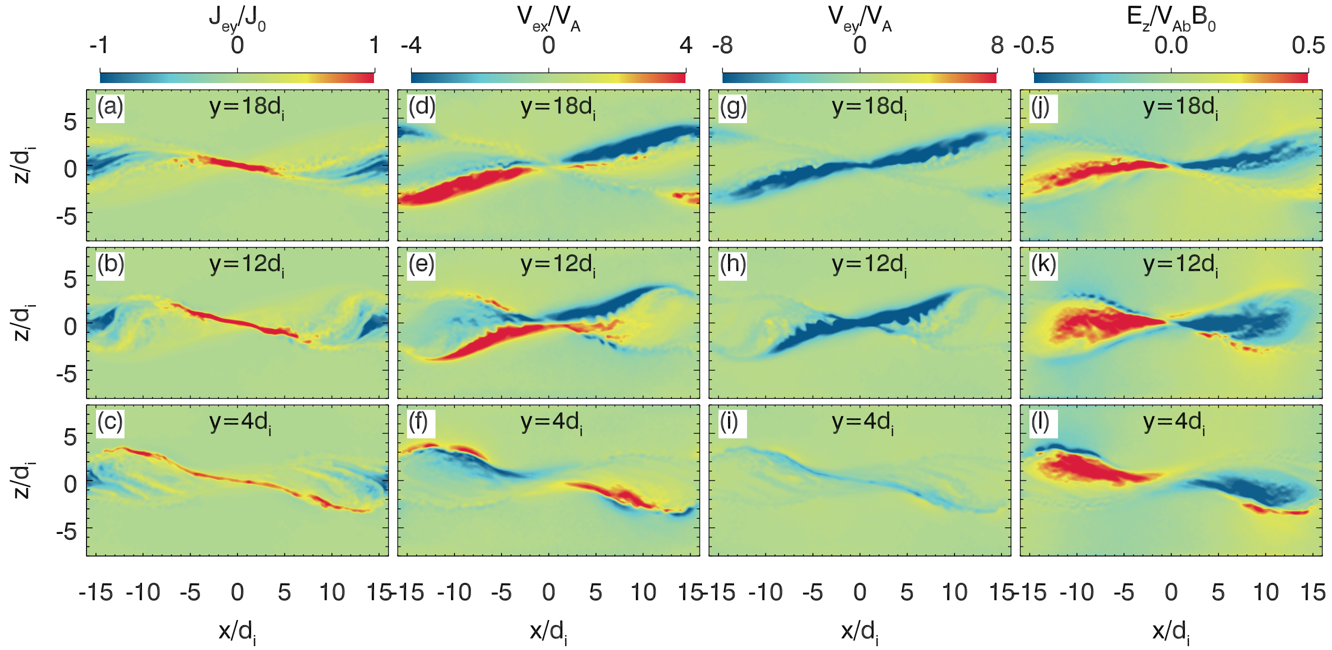

Figure 9. The electron current density J_{ey}/J_0, electron velocity V_{ex}/V_A, V_{ey}/V_A, and electric field $E_z/V_{Ab}B_0$ on the y/d_i = 18, 12, and 4 planes.

showed that the E_z around the x-line points away from the current sheet (Pritchett & Coroniti, 2004), similar to that on the electron drifting side when the x-line has a finite length.

Figure 10 shows the distributions of electron and ion temperatures similar to Figure 6. On the $z = 0$ plane, both electrons and ions are heated in the reconnection region around the x-line. Electron heating is more significant on the electron drifting side, while ion heating is predominant on the ion drifting side, similar to those in the anti-parallel case. In the guide field cases, although the heating is mainly caused by E_y, particles move in the y direction during their parallel motion along the magnetic field, and therefore, the acceleration by the parallel

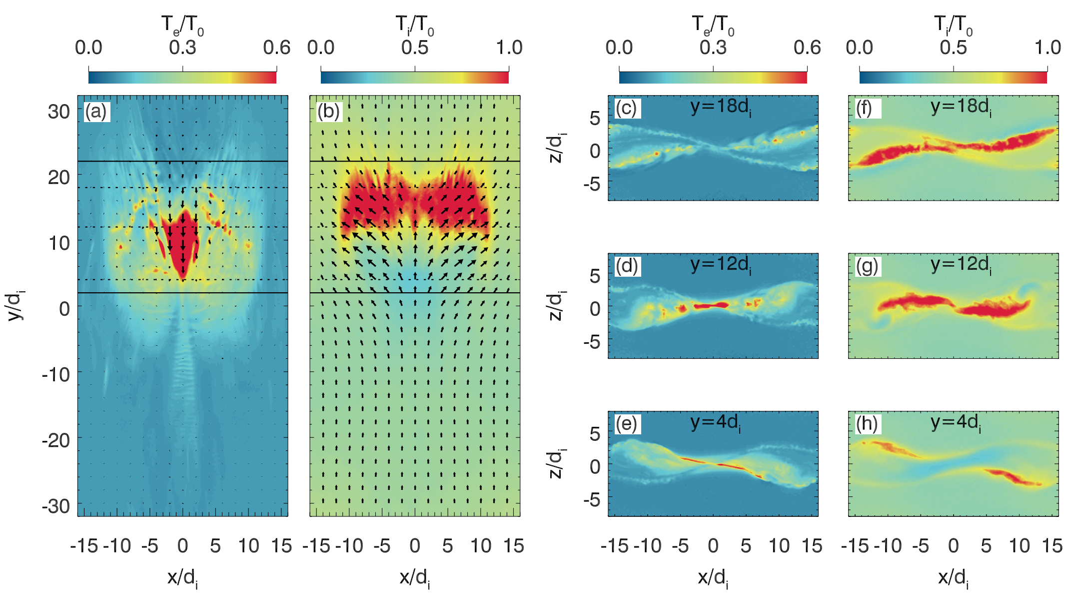

Figure 10. Panels (a) and (b) show the electron and ion temperatures on the $z = 0$ plane, the active reconnection region is bounded by the horizontal solid lines, and the arrows represent the in-plane flow vectors of the associated species. Panels (c)–(h) show the electron and ion temperatures on the y/d_i = 18, 12, and 4 planes, which are labeled by the horizontal dashed lines in panels (a) and (b).

10.1029/2022JA031209

electric field $E_\parallel$ plays an important role in particle heating, especially for electrons (Dahlin et al., 2014). The temperature asymmetry along the y direction can also be observed in the temperature distribution on the $y/d_i = 18$, 12, and 4 planes (panels (c–h)). Furthermore, on the ion drifting side, the heating is more obvious near the upper-right and lower-left separatrices (panels (c) and (f)), while on the electron drifting side, the heating is predominant near the upper-left and lower-right separatrices (panels (e) and (h)).

4. Conclusions and Discussion

In this study, we perform 3D PIC simulations to study the characteristics of magnetic reconnection with a finite x-line length along the current direction. The finite length of the reconnection x-line is achieved by introducing an initial perturbation localized in the current direction in a current sheet with uniform thickness. We consider two cases, anti-parallel reconnection and reconnection with a guide field, and the active reconnection region in both cases extends around $20d_i$ in the y direction when reconnection is well developed (reaches a peak reconnection rate). We find that the characteristics of reconnection are greatly different from those in 2D conditions due to the effects of the finite x-line length. Here we summarize these features as follow:

1. The electron inertia term plays an important role in balancing the reconnection electric field near the two edges of the x-line along the current direction. On the ion drifting side, the amplitude of the electron inertia term is comparable with that of the electron pressure tensor term. On the electron drifting side, the electron inertia term has the different sign with that of the electron pressure tensor term, and cancels some of the contribution of the electron pressure tensor term on the reconnection electric field.
2. On the ion drifting side, ions are heated while the electron heating is not significant. On the electron drifting side, electrons are heated while the ion heating is not significant.
3. During anti-parallel reconnection, the out-of-plane quadrupolar magnetic field B_y has reversed polarization compared with that in 2D conditions on the electron drifting side of the reconnection region. During reconnection with a guide field, the Hall electric field E_z near the x-line points to the current sheet on the ion drifting side, while it points away from the current sheet in other locations along the x-line.

This study has potential applications on localized magnetic reconnection in Earth's magnetotail. Previous observations and simulations have indicated that the x-line of magnetotail reconnection may have a finite length along the dawn-dusk direction (Huang et al., 2015; Liu et al., 2013, 2015; Nakamura et al., 2004, 2005; Pritchett & Lu, 2018; Shay et al., 2003). However, the direct observational evidence is still missing in literature. In this work, we provide key features to identify reconnection of a finite x-line length that can be used for MMS and future missions. The three points summarized above indicate that the characteristics of reconnection, such as the balance of the generalized Ohm's law at the x-line, Hall magnetic/electric field, and ion/electron heating, can be greatly different from those in 2D models, and they are also different between the ion and electron drifting side of the reconnection region. Therefore, these features can be used as identifications for reconnection of a finite x-line length during observations and are helpful for estimating the dawn-dusk location of the satellite relative to the primary reconnection region. The magnetic energy release of one single localized reconnection region with short x-line length ($20 \sim 30d_i$) is too small to meet the requirement of substorm expansion, however, if there are multiple reconnection sites with short x-line length, the energy release will be much larger and may explain the substorm expansion. Furthermore, the results in this work can also apply to the two edges of x-line for reconnection with much longer x-line length.

Previous simulations studied the broadening and shifting of the reconnection region along the current direction (Lapenta et al., 2006; Li et al., 2020; Nakamura et al., 2012; Shay et al., 2003; Shepherd & Cassak, 2012). It is found that the broaden speed of the ion/electron drifting side of the reconnection region is around the ion/electron drifting velocity that carries the current. In our simulation, the initial current is mainly carried by ions, therefore the reconnection region is shifted toward the ion drift direction in both cases. However, the reconnection region does not broaden, the reason might be the different simulation parameters and different method to identify the reconnection region. The evolution of the length of the reconnection region in the current direction is an interesting but complicated problem, it is related to the thickness of the current sheet, the current carrier, and the amplitude of the guide field. This problem is not our focus, in this paper, we care about the characteristics of the reconnection diffusion region when the reconnection x-line has a finite length.

Huang et al. (2020) and Liu et al. (2019) studied reconnection with a finite x-line length using an initial current sheet with varies thickness in the current direction. In their simulations, they found there is a "suppression region" on the dusk side of the active x-line, where the reconnection signatures are weak. The suppression region is characterized by the thicker (ion inertia scale) current sheet compare with that in the active x-line, that has the current sheet thickness on the electron inertia scale. In our study, the thickness of the initial current sheet is uniform and on the ion inertia scale, therefore it is difficult to define the suppression region using the same method. Nevertheless, there are still some interesting features on the ion drifting edge of the x-line in our simulation: the electron drifting velocity increases in the $-y$ direction accompanied by the thinning of the current sheet, and the electron inertia term in the generalized Ohm's law plays a significant role (Figures 3c and 8c). This region serves as a buffer region similar to the suppression region in Huang et al. (2020) and Liu et al. (2019), and is necessary for the development of active reconnection. Because there should be a region on the ion drifting side of the active reconnection x-line that allows the increase of the electron drifting velocity to $\sim V_{Ae}$, which is the typical value for electron velocity in the EDR. It should be noted that this statement is valid in the condition where reconnection develops in an ion scale current sheet with small initial electron drifting velocity. For reconnection in turbulence, the background electron flow velocity can be much larger, and such a buffer region may not be necessary.

Data Availability Statement

The simulation data and scripts used to plot the figures are available at National Space Science Data Center, National Science and Technology Infrastructure of China (https://doi.org/10.57760/sciencedb.06711) (Huang, 2023).

Acknowledgments

This work was supported by the NSFC Grant 42204157, the Fundamental Research Funds for the Central Universities KY2080000088, and WK3420000017. Simulations were performed at National Energy Research Scientific Computing Center (NERSC).

References

Angelopoulos, V., McFadden, J. P., Larson, D., Carlson, C. W., Mende, S. B., Frey, H., et al. (2008). Tail reconnection triggering substorm onset. *Science*, *321*(5891), 931–935. https://doi.org/10.1126/science.1160495

Birn, J., Nakamura, R., Panov, E., & Hesse, M. (2011). Bursty bulk flows and dipolarization in mhd simulations of magnetotail reconnection. *Journal of Geophysical Research*, *116*(A1), A01210. https://doi.org/10.1029/2010ja016083

Bowers, K. J., Albright, B., Yin, L., Bergen, B., & Kwan, T. (2008). Ultrahigh performance three-dimensional electromagnetic relativistic kinetic plasma simulation. *Physics of Plasmas*, *15*(5), 055703. https://doi.org/10.1063/1.2840133

Bowers, K. J., Albright, B. J., Bergen, B., Yin, L., Barker, K. J., & Kerbyson, D. J. (2008). 0.374 pflop/s trillion-particle kinetic modeling of laser plasma interaction on roadrunner. In *Sc'08: Proceedings of the 2008 acm/ieee conference on supercomputing* (pp. 1–11). https://doi.org/10.1109/sc.2008.5222734

Bowers, K. J., Albright, B. J., Yin, L., Daughton, W., Roytershteyn, V., Bergen, B., & Kwan, T. (2009). Advances in petascale kinetic plasma simulation with vpic and roadrunner. *Journal of Physics: Conference Series*, *180*, 012055. https://doi.org/10.1088/1742-6596/180/1/012055

Cassak, P., Liu, Y.-H., & Shay, M. (2017). A review of the 0.1 reconnection rate problem. *Journal of Plasma Physics*, *83*(5), 715830501. https://doi.org/10.1017/s0022377817000666

Chen, P. (2011). Coronal mass ejections: Models and their observational basis. *Living Reviews in Solar Physics*, *8*(1), 1–92. https://doi.org/10.12942/lrsp-2011-1

Dahlin, J., Drake, J., & Swisdak, M. (2014). The mechanisms of electron heating and acceleration during magnetic reconnection. *Physics of Plasmas*, *21*(9), 092304. https://doi.org/10.1063/1.4894484

Daughton, W. (2003). Electromagnetic properties of the lower-hybrid drift instability in a thin current sheet. *Physics of Plasmas*, *10*(8), 3103–3119. https://doi.org/10.1063/1.1594724

Daughton, W., Roytershteyn, V., Karimabadi, H., Yin, L., Albright, B., Bergen, B., & Bowers, K. (2011). Role of electron physics in the development of turbulent magnetic reconnection in collisionless plasmas. *Nature Physics*, *7*(7), 539–542. https://doi.org/10.1038/nphys1965

Eastwood, J., Phan, T., Øieroset, M., & Shay, M. (2010). Average properties of the magnetic reconnection ion diffusion region in the earth's magnetotail: The 2001–2005 cluster observations and comparison with simulations. *Journal of Geophysical Research*, *115*(A8), A08215. https://doi.org/10.1029/2009ja014962

Fujimoto, K. (2016). Three-dimensional outflow jets generated in collisionless magnetic reconnection. *Geophysical Research Letters*, *43*(20), 10–557. https://doi.org/10.1002/2016gl070810

Giovanelli, R. (1946). A theory of chromospheric flares. *Nature*, *158*(4003), 81–82. https://doi.org/10.1038/158081a0

Hesse, M., Neukirch, T., Schindler, K., Kuznetsova, M., & Zenitani, S. (2011). The diffusion region in collisionless magnetic reconnection. *Space Science Reviews*, *160*(1), 3–23. https://doi.org/10.1007/s11214-010-9740-1

Hesse, M., & Schindler, K. (1988). A theoretical foundation of general magnetic reconnection. *Journal of Geophysical Research*, *93*(A6), 5559–5567. https://doi.org/10.1029/ja093ia06p05559

Huang, C., Lu, Q., Lu, S., Wang, P., & Wang, S. (2014). The effect of a guide field on the structures of magnetic islands formed during multiple x line reconnections: Two-dimensional particle-in-cell simulations. *Journal of Geophysical Research: Space Physics*, *119*(2), 798–807. https://doi.org/10.1002/2013ja019249

Huang, K. (2023). Dataset for "characteristics of magnetic reconnection with a finite x-line length" (version v3). Science Data Bank. https://doi.org/10.57760/sciencedb.06711

Huang, K., Liu, Y.-H., Lu, Q., & Hesse, M. (2020). Scaling of magnetic reconnection with a limited x-line extent. *Geophysical Research Letters*, *47*(19), e2020GL088147. https://doi.org/10.1029/2020gl088147

Huang, K., Liu, Y.-H., Lu, Q., Hu, Z., Lynch, K. A., Hesse, M., et al. (2022). Auroral spiral structure formation through magnetic reconnection in the auroral acceleration region. *Geophysical Research Letters*, *49*(18), e2022GL100466. https://doi.org/10.1029/2022gl100466

Huang, S., Fu, H., Vaivads, A., Yuan, Z., Pang, Y., Zhou, M., et al. (2015). Dawn-dusk scale of dipolarization front in the earth's magnetotail: Multi-cases study. *Astrophysics and Space Science*, *357*(1), 1–7. https://doi.org/10.1007/s10509-015-2298-3

Huba, J. (2005). Hall magnetic reconnection: Guide field dependence. *Physics of Plasmas*, *12*(1), 012322. https://doi.org/10.1063/1.1834592

Huba, J., Gladd, N., & Papadopoulos, K. (1977). The lower-hybrid-drift instability as a source of anomalous resistivity for magnetic field line reconnection. *Geophysical Research Letters*, *4*(3), 125–128. https://doi.org/10.1029/gl004i003p00125

Krall, N. A., & Liewer, P. C. (1971). Low-frequency instabilities in magnetic pulses. *Physical Review A*, *4*(5), 2094–2103. https://doi.org/10.1103/physreva.4.2094

Lapenta, G., Krauss-Varban, D., Karimabadi, H., Huba, J., Rudakov, L., & Ricci, P. (2006). Kinetic simulations of x-line expansion in 3d reconnection. *Geophysical Research Letters*, *33*(10), L10102. https://doi.org/10.1029/2005gl025124

Li, T. C., Liu, Y.-H., Hesse, M., & Zou, Y. (2020). Three-dimensional x-line spreading in asymmetric magnetic reconnection. *Journal of Geophysical Research: Space Physics*, *125*(2), e2019JA027094. https://doi.org/10.1029/2019ja027094

Liu, J., Angelopoulos, V., Zhou, X.-Z., Runov, A., & Yao, Z. (2013). On the role of pressure and flow perturbations around dipolarizing flux bundles. *Journal of Geophysical Research: Space Physics*, *118*(11), 7104–7118. https://doi.org/10.1002/2013ja019256

Liu, J., Angelopoulos, V., Zhou, X.-Z., Yao, Z.-H., & Runov, A. (2015). Cross-tail expansion of dipolarizing flux bundles. *Journal of Geophysical Research: Space Physics*, *120*(4), 2516–2530. https://doi.org/10.1002/2015ja020997

Liu, Y.-H., Li, T., Hesse, M., Sun, W., Liu, J., Burch, J., et al. (2019). Three-dimensional magnetic reconnection with a spatially confined x-line extent: Implications for dipolarizing flux bundles and the dawn-dusk asymmetry. *Journal of Geophysical Research: Space Physics*, *124*(4), 2819–2830. https://doi.org/10.1029/2019ja026539

Lu, Q., Huang, C., Xie, J., Wang, R., Wu, M., Vaivads, A., & Wang, S. (2010). Features of separatrix regions in magnetic reconnection: Comparison of 2-d particle-in-cell simulations and cluster observations. *Journal of Geophysical Research*, *115*(A11), A11208. https://doi.org/10.1029/2010ja015713

Masuda, S., Kosugi, T., Hara, H., Tsuneta, S., & Ogawara, Y. (1994). A loop-top hard x-ray source in a compact solar flare as evidence for magnetic reconnection. *Nature*, *371*(6497), 495–497. https://doi.org/10.1038/371495a0

Nagai, T., Shinohara, I., Fujimoto, M., Hoshino, M., Saito, Y., Machida, S., & Mukai, T. (2001). Geotail observations of the hall current system: Evidence of magnetic reconnection in the magnetotail. *Journal of Geophysical Research*, *106*(A11), 25929–25949. https://doi.org/10.1029/2001ja900038

Nakamura, R., Baumjohann, W., Mouikis, C., Kistler, L., Runov, A., Volwerk, M., et al. (2004). Spatial scale of high-speed flows in the plasma sheet observed by cluster. *Geophysical Research Letters*, *31*(9), L09804. https://doi.org/10.1029/2004gl019558

Nakamura, R., Baumjohann, W., Mouikis, C., Kistler, L., Runov, A., Volwerk, M., et al. (2005). Multi-point observation of the high-speed flows in the plasma sheet. *Advances in Space Research*, *36*(8), 1444–1447. https://doi.org/10.1016/j.asr.2005.05.101

Nakamura, T., Nakamura, R., Alexandrova, A., Kubota, Y., & Nagai, T. (2012). Hall magnetohydrodynamic effects for three-dimensional magnetic reconnection with finite width along the direction of the current. *Journal of Geophysical Research*, *117*(A3), A03220. https://doi.org/10.1029/2011ja017006

Øieroset, M., Phan, T., Fujimoto, M., Lin, R., & Lepping, R. (2001). In situ detection of collisionless reconnection in the earth's magnetotail. *Nature*, *412*(6845), 414–417. https://doi.org/10.1038/35086520

Pritchett, P. (2001). Geospace environment modeling magnetic reconnection challenge: Simulations with a full particle electromagnetic code. *Journal of Geophysical Research*, *106*(A3), 3783–3798. https://doi.org/10.1029/1999ja001006

Pritchett, P. (2016). Three-dimensional structure and kinetic features of reconnection exhaust jets. *Journal of Geophysical Research: Space Physics*, *121*(1), 214–226. https://doi.org/10.1002/2015ja022053

Pritchett, P., & Coroniti, F. (2010). A kinetic ballooning/interchange instability in the magnetotail. *Journal of Geophysical Research*, *115*(A6), A06301. https://doi.org/10.1029/2009ja014752

Pritchett, P., Coroniti, F., & Nishimura, Y. (2014). The kinetic ballooning/interchange instability as a source of dipolarization fronts and auroral streamers. *Journal of Geophysical Research: Space Physics*, *119*(6), 4723–4739. https://doi.org/10.1002/2014ja019890

Pritchett, P., & Coroniti, F. V. (2004). Three-dimensional collisionless magnetic reconnection in the presence of a guide field. *Journal of Geophysical Research*, *109*(A1), A01220. https://doi.org/10.1029/2003ja009999

Pritchett, P., & Lu, S. (2018). Externally driven onset of localized magnetic reconnection and disruption in a magnetotail configuration. *Journal of Geophysical Research: Space Physics*, *123*(4), 2787–2800. https://doi.org/10.1002/2017ja025094

Ricci, P., Brackbill, J., Daughton, W., & Lapenta, G. (2004). Collisionless magnetic reconnection in the presence of a guide field. *Physics of Plasmas*, *11*(8), 4102–4114. https://doi.org/10.1063/1.1768552

Rong, Z., Ding, Y., Slavin, J., Zhong, J., Poh, G., Sun, W., et al. (2018). The magnetic field structure of mercury's magnetotail. *Journal of Geophysical Research: Space Physics*, *123*(1), 548–566. https://doi.org/10.1002/2017ja024923

Shay, M., Drake, J., Swisdak, M., Dorland, W., & Rogers, B. (2003). Inherently three dimensional magnetic reconnection: A mechanism for bursty bulk flows? *Geophysical Research Letters*, *30*(6), 1345. https://doi.org/10.1029/2002gl016267

Shepherd, L., & Cassak, P. (2012). Guide field dependence of 3-dx-line spreading during collisionless magnetic reconnection. *Journal of Geophysical Research*, *117*(A10), A10101. https://doi.org/10.1029/2012ja017867

Shibata, K., Masuda, S., Shimojo, M., Hara, H., Yokoyama, T., Tsuneta, S., et al. (1995). Hot-plasma ejections associated with compact-loop solar flares. *The Astrophysical Journal*, *451*(2), L83. https://doi.org/10.1086/309688

Sun, W., Dewey, R. M., Aizawa, S., Huang, J., Slavin, J. A., Fu, S., et al. (2021). Review of mercury's dynamic magnetosphere: Post-messenger era and comparative magnetospheres. *Science China Earth Sciences*, 1–50. https://doi.org/10.1007/s11430-021-9828-0

Sun, W., Fu, S., Slavin, J., Raines, J., Zong, Q., Poh, G., & Zurbuchen, T. (2016). Spatial distribution of mercury's flux ropes and reconnection fronts: Messenger observations. *Journal of Geophysical Research: Space Physics*, *121*(8), 7590–7607. https://doi.org/10.1002/2016ja022787

Vasyliunas, V. M. (1975). Theoretical models of magnetic field line merging. *Reviews of Geophysics*, *13*(1), 303–336. https://doi.org/10.1029/rg013i001p00303

Wang, L., Huang, C., Du, A., & Ge, Y. (2022). Hall nature ahead of dipolarization fronts in the earth's magnetotail: A statistical study for mms data. *Geophysical Research Letters*, *49*(3), e2021GL097075. https://doi.org/10.1029/2021gl097075

Wu, P., & Shay, M. (2012). Magnetotail dipolarization front and associated ion reflection: Particle-in-cell simulations. *Geophysical Research Letters*, *39*(8), L08107. https://doi.org/10.1029/2012gl051486

Zenitani, S., Hesse, M., Klimas, A., & Kuznetsova, M. (2011). New measure of the dissipation region in collisionless magnetic reconnection. *Physical Review Letters*, *106*(19), 195003. https://doi.org/10.1103/physrevlett.106.195003